The
University
Of
Sheffield.

This is a repository copy of *Design of a split Hopkinson pressure bar with partial lateral confinement*.

White Rose Research Online URL for this paper:
http://eprints.whiterose.ac.uk/105921/

Version: Accepted Version

White Rose
university consortium
Universities of Leeds, Sheffield & York

eprints@whiterose.ac.uk
https://eprints.whiterose.ac.uk/

Design of a split Hopkinson pressure bar with partial lateral confinement

Andrew D. Barr[a*], Sam D. Clarke[a], Sam E. Rigby[a], Andrew Tyas[a,b], James A. Warren[a,b]

[a]Department of Civil and Structural Engineering, The University of Sheffield,
Mappin Street, Sheffield, S1 3JD, UK.
[b]Blastech Ltd., The BioIncubator, 40 Leavygreave Road, Sheffield, S3 7RD, UK.
*Email: a.barr@shef.ac.uk

Abstract

This paper presents the design of a modified split Hopkinson pressure bar (SHPB) where partial lateral confinement of the specimen is provided by the inertia of a fluid annulus contained in a long steel reservoir. In contrast to unconfined testing, or a constant cell pressure applied before axial loading, lateral restraint is permitted to develop throughout the axial loading: this enables the high-strain-rate shear behaviour of soils to be characterised under conditions which are more representative of buried explosive events. A pressure transducer located in the wall of the reservoir allows lateral stresses to be quantified, and a dispersion-correction technique is used to provide accurate measurements of axial stress and strain. Preliminary numerical modelling is utilised to inform the experimental design, and the capability of the apparatus is demonstrated with specimen results for a dry quartz sand.

Keywords: Experimental design; partial confinement; split Hopkinson pressure bar

1 Introduction

Widespread use of improvised explosive devices in current conflicts has driven a need to understand the role of soils in buried explosive events. The design of effective protective solutions requires accurate predictions of the blast loading produced in these events, which has been shown in large-scale field tests to be greatly influenced by the properties of the surrounding soil [1–5]. The ability to define yield surfaces at high pressures and strain rates is a key component in developing a robust constitutive model of soil behaviour under extreme loading, and so a reliable means of testing soils triaxially under these conditions is required.

The split Hopkinson pressure bar (SHPB) is commonly used to investigate the response of materials at strain rates of $10^2 \, \text{s}^{-1}$ to $10^4 \, \text{s}^{-1}$, and tests on soils using the SHPB are typically carried out by confining a soil specimen in a rigid tube or ring, which restricts lateral deformation. These uniaxial strain tests are useful for characterising the compaction response of soil at varying strain rates [6–8] and comparing soils with varying moisture contents [8, 9], initial densities [10, 11] and particle size distributions [12], but cannot be used to describe the yield surface, as shear failure cannot occur.

Several authors have developed methods which allow the lateral confinement of a SHPB specimen to be modified to provide a triaxial stress state, and a number of these are based on an adaptation of the rigid

1

confinement condition. Pierce and Charlie [13] investigated the wave speed of partially-saturated sand at confining stresses of 0 kPa and 310 kPa using a steel tube lined with a membrane. While the steel tube prevented the development of lateral strains, water pressure applied between the tube and membrane provided an additional confining stress, which was also applied along the pressure bars through use of a piston assembly on the transmitter bar. Bailly et al. [14] made use of brass confining rings which approximated elastic–perfectly-plastic behaviour at high strain rates. Tests specimens deformed approximately in uniaxial strain until the radial stress reached the yield stress in the ring, after which the specimen was permitted to deform laterally at a quasi-constant confining stress.

Other authors have adapted the use of the triaxial cell to high-strain-rate testing. Christensen et al. [15] performed triaxial tests on sandstone to confining stresses of 207 MPa using a long pressure vessel. The pressure vessel contained the specimen and pressure bars, with an opening at one end to allow loading of the incident bar, which was secured with a collar. Similar experiments were carried out on basalt by Lindholm et al. [16], who used a shorter pressure vessel around the rock specimen in conjunction with a hydraulic actuator on the end of the transmitter bar to apply hydrostatic stresses of up to 690 MPa. Frew et al. [17] adapted the triaxial SHPB further to use pressure vessels around both the specimen and transmitter bar end. This apparatus was used by Martin et al. [18] to characterise the shear response of sand at confining stresses between 25 MPa and 150 MPa, where a method was also developed to record the axial and radial deformation of the specimen during hydrostatic loading.

The methods employed by Christensen et al. [15], Lindholm et al. [16] and Martin et al. [18] have been successfully used to perform dynamic conventional triaxial compression (CTC) tests, where hydrostatic loading is followed by a high-strain-rate deviatoric phase. The current work seeks to understand the shear behaviour of soils in explosive events, where a soil may deform uniaxially before developing significant lateral confinement, which is also influenced by the inertia of the surrounding soil. Quantification of this inertial effect in a soil specimen with a developing stress state requires a departure from the CTC techniques which are currently available, and so a new apparatus has been developed to allow a confining stress to develop passively during high-strain-rate axial loading. This partial lateral confinement falls between unconfined testing, where the specimen deforms under uniaxial stress, and CTC testing, where a constant cell pressure is maintained throughout.

2   Experimental setup

The modified SHPB consists of a typical pressure bar arrangement with the addition of a 600 mm long steel water reservoir, which is mounted in linear bearings and centred around the specimen as shown in Figure 1a. With the pressure bars in position an annular void exists along the length of the reservoir, which is filled with water at atmospheric pressure, as in Figure 1b. Saturation of a soil specimen is prevented through use of a 0.4 mm thick latex membrane, which is sealed against the pressure bars using o-rings. When the specimen is loaded axially, radial deformation is resisted by the inertia of the water annulus: this radial resistance develops in response to the behaviour of the specimen, and is measured by a pressure transducer positioned in the wall of the reservoir.

To ensure that the recorded pressure is representative of the radial stress on the surface of the specimen, numerical modelling of the reservoir was used to select the length and internal diameter of the reservoir, as described in Section 3. The reservoir length was chosen so that the time for a stress wave initiated at the specimen surface to travel to and from the end of the reservoir exceeds the loading duration in the specimen,
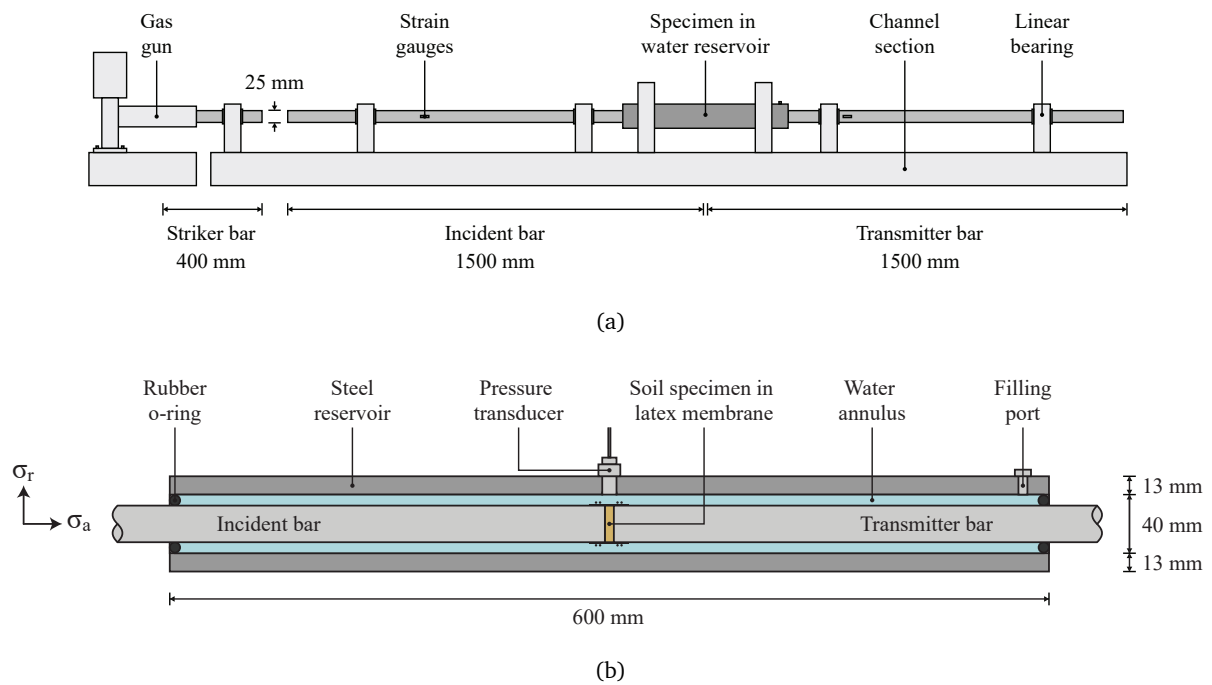
(a)

(b)

Figure 1: Schematic of the partially confined split Hopkinson pressure bar apparatus with a soil specimen: a) Bar and reservoir arrangement, b) Water reservoir section with axial/radial axis convention.

MAT_NULL							
ρ_0							
1000							

EOS_LINEAR_POLYNOMIAL							
C_0	C_1	C_2	C_3	C_4	C_5	C_6	E_0
0.0	2.190E9	9.224E9	8.767E9	0.4934	1.3937	0.0	205.36E3

Table 1: Material model and equation of state parameters for water (SI units) [19]

ensuring that inward-travelling waves from the boundary do not interfere with the pressure measurements. This also allows simplification of the seals between the reservoir and the pressure bars, which are only required to retain the water at atmospheric pressure.

3 Preliminary modelling

3.1 Model setup

Numerical analyses of the arrangement shown in Figure 1 were conducted using the explicit FE code LS-DYNA [20] in order to test the efficacy of measuring the dynamic fluid pressure as an indicator of the radial confining stress acting on the sample, and to investigate the effect of reservoir length and inner radius (i.e. thickness of fluid annulus). As the purpose of the numerical modelling is to prove the concept of the apparatus and to explore the required geometry of the reservoir, it is sufficient to simulate scenarios with indicative sample material properties in order to inform the experimental design and allow more sophisticated material model parameters to eventually be gathered.

The steel pressure bars were modelled as linear elastic with a density, Young's modulus and Poisson's ratio of $\rho = 7850\,\mathrm{kg\,m^{-3}}$, $E = 200\,\mathrm{GPa}$ and $\nu = 0.3$ respectively. The geometry of the pressure bars was as shown in Figure 1a. The striker bar was given an impact velocity of $5\,\mathrm{m\,s^{-1}}$ and a sample length of 5 mm was chosen for all analyses. The sample was also modelled as a linear elastic material, with 'typical' rubber material properties, i.e. $\rho = 1000\,\mathrm{kg\,m^{-3}}$, $E = 100\,\mathrm{MPa}$ and $\nu = 0.5$, in order to generate large radial strains within the sample and induce a large fluid pressure within the reservoir. The water was modelled using the linear polynomial equation of state:

$$P = C_0 + C_1\mu + C_2\mu^2 + C_3\mu^3 + (C_4 + C_5\mu + C_6\mu^2)E \tag{1}$$

where $C_0, C_1, C_2, C_3, C_4, C_5$ and C_6 are constants, $\mu = \rho/\rho_0 - 1$, ρ and ρ_0 are the current and initial densities of the fluid, and E is the specific internal energy of the fluid. The null material properties (of which only density is required) and equation of state parameters used for water in this study are shown in Table 1. The initial internal energy of the water, E_0, was specified as 205.36 kPa to pressurise the water to atmospheric conditions (101 kPa atmospheric pressure).

The model was discretised using axi-symmetric Lagrangian shell elements with 0.5 mm side lengths, with the mesh size informed by the results of a mesh sensitivity analysis which is not included here for brevity. Automatic 2D surface-to-surface contact was specified between all parts. The reservoir was varied in length
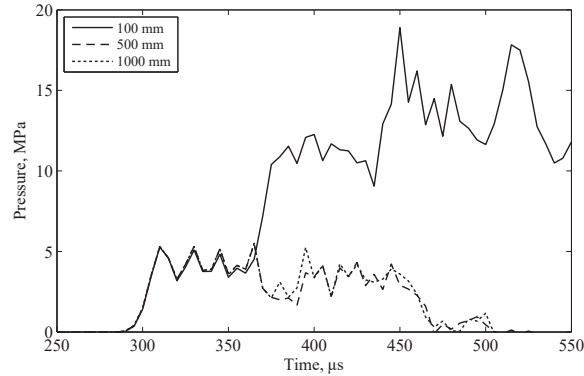
4

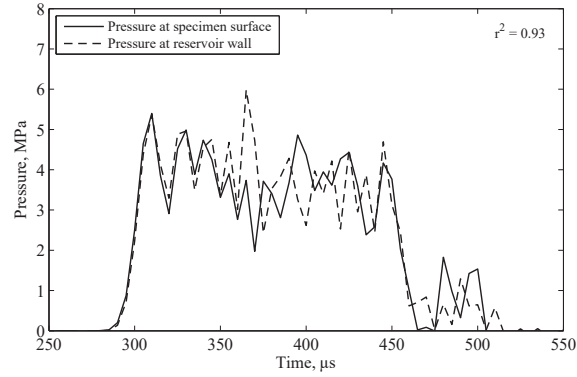Figure 2: Effect of reservoir length on pressure at wall of reservoir.

between 100 mm and 1000 mm, and was varied in internal radius between 17.5 mm and 37.5 mm. For simplicity, the steel reservoir was modelled as a rigid boundary, assuming that the fluid pressures generated will not be large enough to cause significant radial strains in the reservoir. The o-ring seals were also modelled as a rigid boundary, as edge reflections will not affect the pressure transducer measurements until after the axial loading is completed given a sufficiently long reservoir.
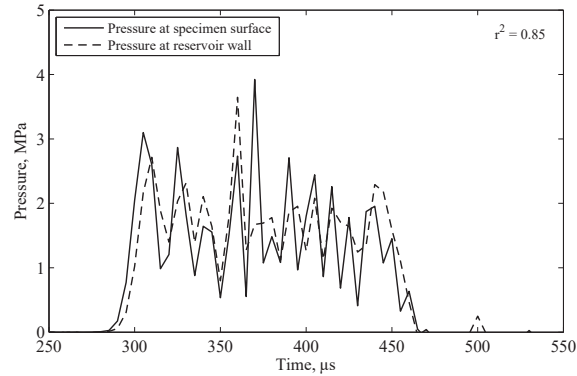
3.2   Effect of reservoir length

To test the effect of the length of reservoir, three analyses were run with a reservoir radius of 17.5 mm and lengths of 100 mm, 500 mm and 1000 mm, centred around the sample. Results of these analyses are shown in Figure 2. For the 100 mm long reservoir, inward-travelling waves from the remote ends begin to contaminate the results at approximately 370 μs. The traces for the 500 mm and 1000 mm reservoirs are not affected by these reflected waves, and are almost identical. Assuming a wavespeed of 1484 m s^{-1} in the water, a reservoir length of 500 mm gives the potential to record a loading event with a duration of 337 μs before any inward-travelling waves from the remote boundary of the reservoir can affect the recordings. For the current pressure bar setup the reservoir is therefore required to be at least 500 mm in length.
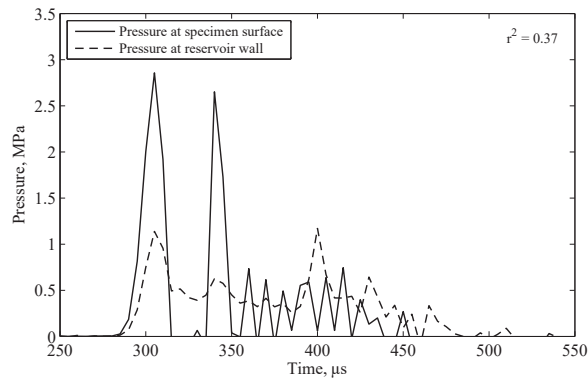
3.3   Effect of reservoir inner radius

Following on from this, the reservoir length was set at 500 mm and analyses were run with inner radii of 17.5 mm, 22.5 mm and 37.5 mm, giving distances from the sample edge to the wall of the reservoir (fluid annulus thickness) of 5 mm, 10 mm and 25 mm respectively. Results of these analyses are shown in Figure 3. For the 17.5 mm inner radius reservoir, there is a near-perfect match ($r^2 = 0.93$) between the pressure in the elements at the sample edge and the at the reservoir wall. The agreement is less precise, but still acceptable ($r^2 = 0.85$), for the 22.5 mm case, where the increased fluid thickness reduced the confining stress generated in the specimen. For the 37.5 mm case, the time taken for the pressure wave to propagate from the sample to the edge of the reservoir is no longer negligible compared to the loading duration, leading to a delay in the development of the pressure at the reservoir wall (Figure 3c). The pressure recorded at the wall of the reservoir cannot therefore be said to be an accurate representation of the pressure directly adjacent to the

Figure 3: Effect of reservoir width on difference between water pressure at sample face and water pressure at wall of reservoir for inner radii of (a) 17.5 mm, (b) 22.5 mm, and (c) 37.5 mm

sample in this case ($r^2 = 0.37$). To ensure that the pressure transducer reading is accurate, the inner radius of the reservoir will be no larger than 22.5 mm.

3.4 Reservoir dimensions

Following these analyses, a 600 mm length, 20 mm inner radius and 33 mm outer radius were adopted for the reservoir. As the reservoir is longer than 500 mm and has an inner radius less than 22.5 mm, the fluid pressure recorded at the pressure gauge embedded in the inner wall of the reservoir will be an accurate measure of the sample confining stress. A sufficiently large wall thickness (13 mm) was selected to ensure the reservoir behaves as an effectively rigid boundary.

4 Sample methodology

To demonstrate the capability of the partially-confined SHPB, and to verify that the selected design leads to accurate measurements of fluid pressure, an experiment was carried out on a dry soil specimen. The soil was a uniform fine and medium sand (EN ISO 14688–1:2002), with a mean particle size of 250 μm and a coefficient of uniformity, C_u of 2.2. Installation of the specimen into the water reservoir was as follows, where numbers refer to the annotations in Figure 4.

1. The o-ring seals for the water reservoir were fitted to the incident and transmitter bars.

2. The water reservoir was installed by temporarily unbolting and translating the bearing on the incident bar.

3. A sand specimen was installed between the incident and transmitter bars. In this experiment the specimen was held in position, and isolated from the fluid annulus, by a thin polythene membrane: future experiments will use a bespoke latex membrane. The specimen was prepared with a nominal length of 5 mm and a diameter of 25 mm.

4. Once installed, the specimen length was measured accurately using a travelling microscope fitted with a digital dial gauge, enabling the initial density the soil to be calculated. The precise location of the end of a pressure bar is difficult to discern through a microscope, and so shallow grooves were cut into the circumference of each bar as benchmarks, as shown in Figure 5. The difference in length between the benchmarks before and after the specimen was installed was used to infer the initial length of the specimen, and so the benchmarks were cut using a chisel-edged bit on a lathe so that they provided well-defined edges.

5. The water reservoir was translated into position, and the pressure port was aligned with the centre of specimen using an additional set of lathed grooves.

6. The incident bar bearing was returned to its test position and bolted down.

7. The o-rings were inserted into the water reservoir to seal its ends.

8. The water reservoir was filled with water using the filling port and sealed by fitting the pressure transducer and filling port bolt. The transducer used in this experiment was a Kulite HKM–375–2500, calibrated by the manufacturer to perform linearly to a pressure of 25 MPa.
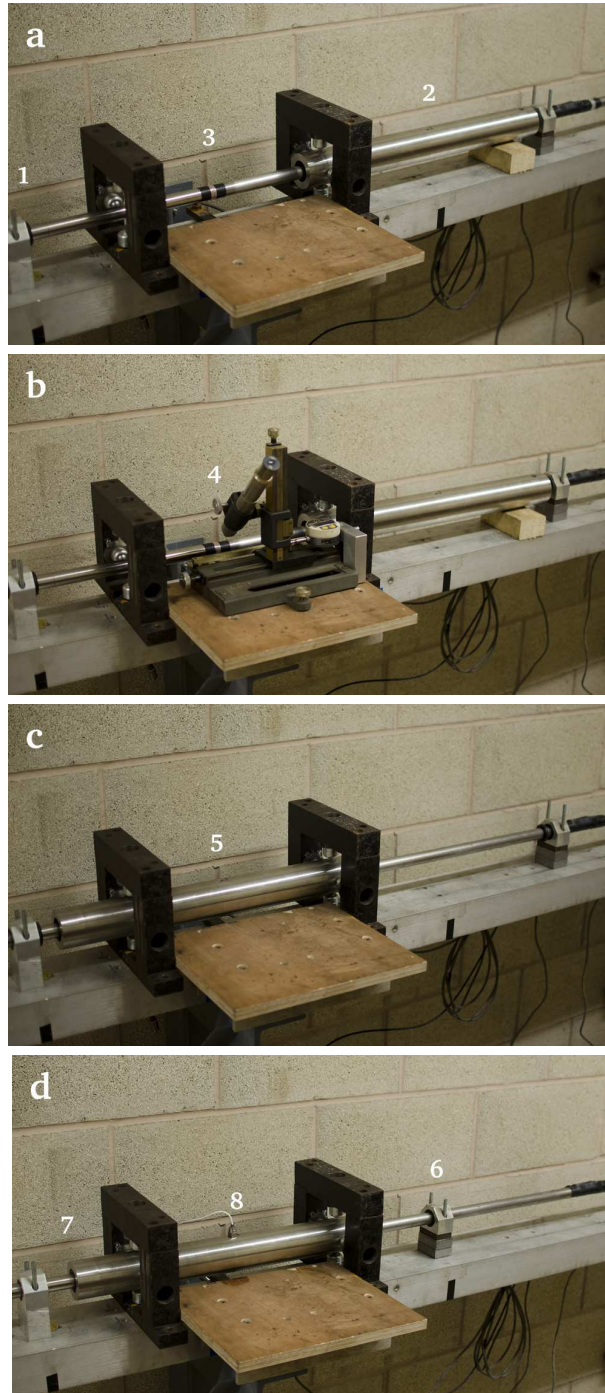
Figure 4: Water reservoir methodology: a) specimen installation, b) specimen measurement, c) water reservoir alignment, d) water reservoir seals and instrumentation.
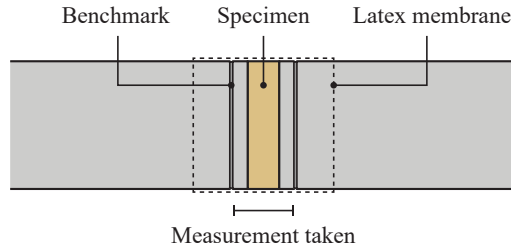
Figure 5: Lathe-cut benchmarks used to measure the initial specimen length.

The method then proceeded as in a conventional SHPB experiment. Loading was provided by firing a steel striker bar from a gas gun to impact the incident bar ($v_{\text{striker}} \approx 20\,\text{m\,s}^{-1}$), and signals from the pressure bar strain gauges and pressure transducer were recorded using a TiePie Handyscope four-channel digital oscilloscope, using 14-bit resolution and a sampling rate of 1.562 MHz.

The inertial forces which dominate the early stages of loading are a key topic of interest in the current study, and so no attempt was made to modify the incident stress wave through the use of pulse shapers [18]. This necessarily means that the strain rate varies during the experiment, as shown in Figure 6, where the strain rate increases from zero to $3400\,\text{s}^{-1}$ over approximately 50 µs.

5   Signal processing

In processing the signals from SHPB experiments it is often assumed that longitudinal stress waves in the pressure bars propagate one-dimensionally at a common velocity c_0, and so measurements taken at the strain gauges are often simply translated to the end of the bar using a suitable time delay [21]. In reality, stress waves propagate at a specific phase velocity, c_P, which is a function of frequency and the bar's diameter, one-dimensional wave speed and Poisson's ratio, as shown in Figure 7 [22]. Phase velocity decreases as the frequency of a wave increases, leading to dispersion of a signal as it propagates down the bar. Dispersion of the stress pulse is accompanied by a frequency-dependent variation in stress and strain across the bar cross-section, so that a signal recorded on the surface of the bar at some distance from the specimen will not accurately describe the stresses the specimen was subjected to, and hence cannot be used to accurately determine the specimen response.

To ensure that the inferred measurements of axial stress and strain accurately represent the specimen behaviour, the pressure bar signals were processed using an implementation of the dispersion-correction method described by Tyas and Pope [23]. In this method:

1. The time-domain strain signal is converted into the frequency domain using the fast Fourier transform (FFT).

2. A correction is applied to the phase angle of each frequency component to account for the dispersion over the distance between the strain gauge and the bar end, arising from the relationship shown in Figure 7.

3. A correction is applied to the amplitude of each frequency component using the factors M_1 and M_2, which account for the variation of strain and Young's modulus across the bar cross section, respectively.
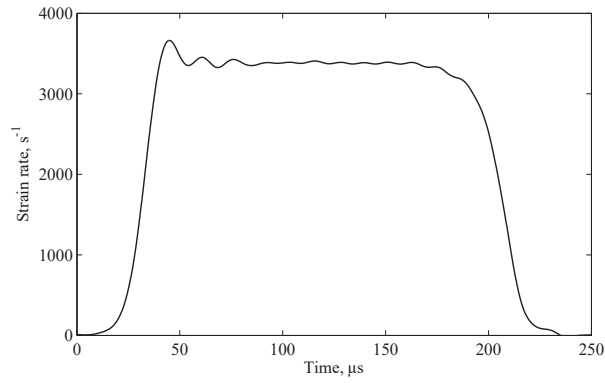
9

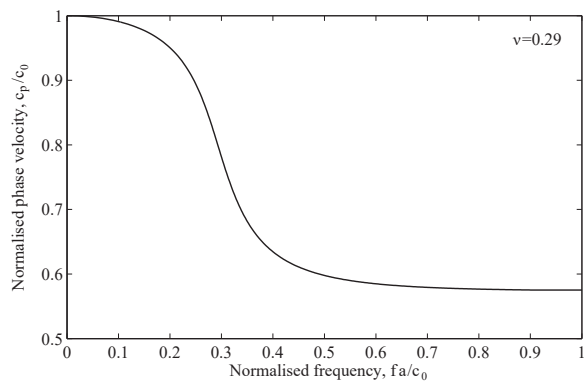Figure 6: Variation of strain rate during a partially-confined experiment on dry quartz sand.

Figure 7: Relationship of phase velocity to frequency for the first mode of propagation of a longitudinal wave.
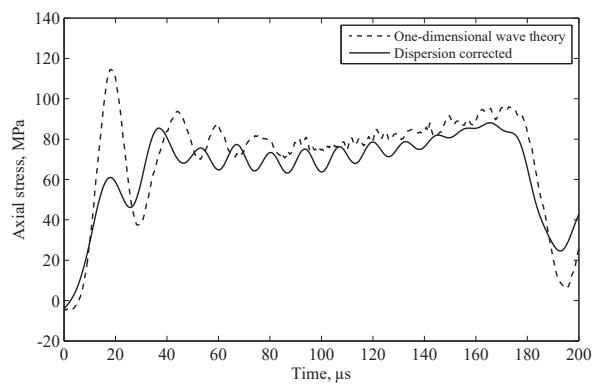

Figure 8: Incident bar stress calculated using one-dimensional wave theory and a dispersion-corrected method.
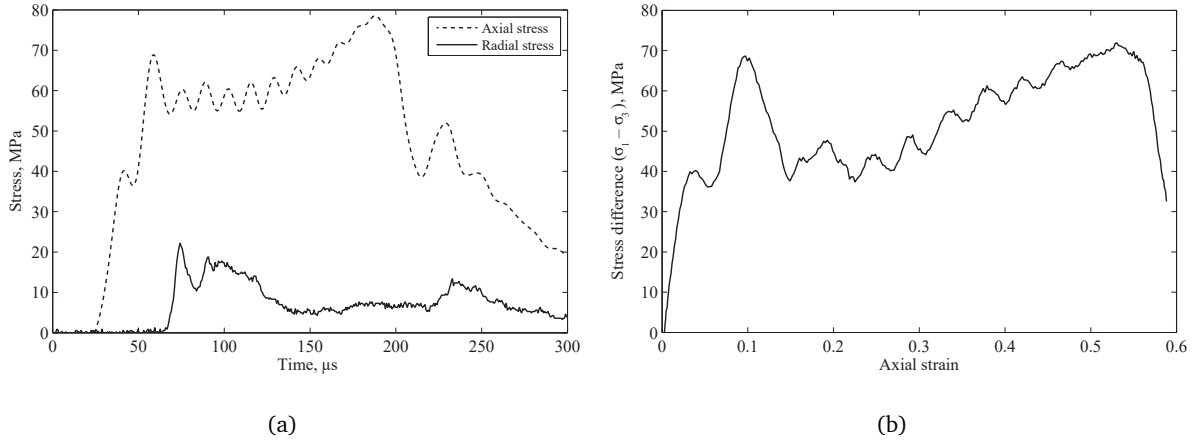
Figure 9: Partially-confined SHPB experiment on dry quartz sand: a) Axial and radial stresses, b) Axial stress–strain response.

These are derived from Davies' analysis of the radial effects in a cylindrical pressure bar [24].

4. The signal is transformed back into the time domain using the inverse FFT.

This dispersion correction is particularly important in inferring the stress transmitted into the specimen from the incident bar, as it is calculated from the sum of the incident and reflected waves, which both contain significant high-frequency components. Using one-dimensional wave theory the incident and reflected stress waves measured at the incident bar strain gauge are assumed to maintain their shape as they are translated along the time axis, while in the corrected method the dispersion associated with 1000 mm of travel in the bar is added to the incident wave and removed from the reflected wave. This is illustrated in Figure 8, where the dispersion-corrected method reduces the amplitude of the stress wave and removes a large initial oscillation in stress, which could have otherwise led to erroneous conclusions on the behaviour of the specimen.

6 Sample results

The recorded axial (σ_1) and radial (σ_3) stresses are shown in Figure 9a, where the axial stress is the mean of the stresses acting on each specimen face. The transit time from the specimen to the pressure transducer through the water annulus (5.1 μs, assuming a wavespeed in water of $1482 \, \mathrm{m\,s^{-1}}$) was taken into account when analysing the radial stress in the specimen. The pressure transducer provided excellent measurements of radial stress, which correspond well with the features in the recorded axial stress. Of particular note is the first 40 μs of the axial stress pulse, where the specimen deforms without any measured radial stress on the surface of the specimen, resulting in a peak in the stress difference ($\sigma_1 - \sigma_3$) in Figure 9b. A similar lag in measurements of radial stress has been observed in confined SHPB experiments [8], and was attributed to the effects of radial inertia in the sand specimen. This behaviour and the effects of inertia will be investigated in more detail in future test series using the water reservoir.

11

7   Discussion

It was noted in Section 3.3 that the radial confinement generated in the specimen is a function of the internal radius of the reservoir: as the thickness of the fluid annulus increases, the radial confinement decreases. The apparatus can therefore be used to investigate the shear behaviour of soils at a range of confining stresses by using a number of reservoirs with varying internal diameters.

The preliminary modelling indicated that the maximum internal radius for reliable confining stress measurements was 22.5 mm. The minimum internal radius is limited by the requirement to move the reservoir into position without disturbing the specimen, and is likely to be on the order of 15 mm. The magnitude of the confining stress using these geometries will depend on the behaviour of a particular specimen under a specific axial loading.

The ability to analyse the partially-confined behaviour of soils in this way bridges the gap between nominally unconfined experiments (using a thin friable membrane) and fully-confined experiments (using a rigid steel ring), and these three experimental methods can be used together to provide a full picture of the behaviour of soils during high-strain-rate blast and impact events.

Future test series using this new apparatus will be used to define high-strain-rate yield surfaces for a series of soils, which will enable any strain-rate dependent behaviour to be identified, including the quantification of radial inertial effects. This will be aided by comparison of the observed behaviour with results from high-pressure quasi-static triaxial tests [25]. The effects of soil parameters such as moisture content, initial density, particle size distribution and angularity on this shear behaviour will also be investigated, enabling mechanisms to be proposed for the observed variation in loading from buried explosive events.

8   Summary

A methodology for partially-confined SHPB experiments has been presented where the specimen is restrained laterally by the inertia of a fluid annulus contained in a long steel reservoir. As lateral restraint is allowed to develop in response to the axial stress pulse rather than being applied as a quasi-static cell pressure, this approach is more appropriate than existing dynamic conventional triaxial compression experiments for representing explosive events in soils.

A pressure transducer in the wall of the reservoir is used to measure the radial stress in the specimen. Numerical modelling was performed to select the dimensions of the reservoir to ensure that internal reflections do not affect the stress measurements, and so the radial stress on the surface of the specimen will be accurately represented. The use of the partially-confined SHPB was demonstrated on a dry specimen of quartz sand, and excellent measurements of axial and radial stress were recorded.

This apparatus will enable the shear response of soils in buried explosive events to be characterised under more indicative stress states than can be achieved using existing techniques, and so the resulting increase in the accuracy of numerical models of these events will be of great benefit to the development of systems to protect against buried explosive threats.

9   Acknowledgements

References

[1] S D Clarke, S D Fay, J A Warren, A Tyas, S E Rigby, J J Reay, R Livesy, and I Elgy. Geotechnical causes for variations in output measured from shallow buried charges. *International Journal of Impact Engineering*, 86:274–283, 2015.

[2] S D Clarke, S D Fay, J A Warren, A Tyas, S E Rigby, J J Reay, R Livesy, and I Elgy. Predicting the role of geotechnical parameters on the output from shallow buried explosives. *Submitted for publication in International Journal of Impact Engineering*, 2016.

[3] S E Rigby, S D Fay, S D Clarke, A Tyas, J J Reay, J A Warren, M Gant, and I Elgy. Measuring spatial pressure distribution from explosives buried in dry Leighton Buzzard sand. *Submitted for publication in International Journal of Impact Engineering*, 2016.

[4] D M Fox, X Huang, D Jung, W L Fourney, U Leiste, and J S Lee. The response of small scale rigid targets to shallow buried explosive detonations. *International Journal of Impact Engineering*, 38(11):882–891, 2011.

[5] D M Fox, S A Akers, U H Leiste, W L Fourney, J E Windham, J S Lee, J Q Ehrgott, and L C Taylor. The effects of air filled voids and water content on the momentum transferred from a shallow buried explosive to a rigid target. *International Journal of Impact Engineering*, 69:182–193, 2014.

[6] A M Bragov, A K Lomunov, I V Sergeichev, K Tsembelis, and W G Proud. Determination of physicomechanical properties of soft soils from medium to high strain rates. *International Journal of Impact Engineering*, 35(9):967–976, 2008.

[7] B Song, W Chen, and V Luk. Impact compressive response of dry sand. *Mechanics of Materials*, 41:777–785, 2009.

[8] A D Barr, S D Clarke, M Petkovski, A Tyas, S E Rigby, J Warren, and S Kerr. Effects of strain rate and moisture content on the behaviour of sand under one-dimensional compression. *Experimental Mechanics*, 2016.

[9] B E Martin, W Chen, B Song, and S Akers. Moisture effects on the high strain-rate behavior of sand. *Mechanics of Materials*, 41(6):786–798, 2009.

[10] H Lu, H Luo, and R Komaduri. Dynamic compressive response of sand under confinements. In *Proceedings of the SEM Annual Conference*, pages 9–15, Albuquerque, NM, USA, 2009.

[11] H Luo, H Lu, W L Cooper, and R Komanduri. Effect of mass density on the compressive behavior of dry sand under confinement at high strain rates. *Experimental Mechanics*, 51(9):1499–1510, 2011.

[12] J Huang, S Xu, and S Hu. Effects of grain size and gradation on the dynamic responses of quartz sands. *International Journal of Impact Engineering*, 59:1–10, 2013.

[13] S J Pierce and W A Charlie. *High-intensity compressive stress wave propagation through unsaturated sands*. PhD thesis, Geotechnical Engineering Program, Colorado State University, USA, 1990.

[14] P Bailly, F Delvare, J Vial, J L Hanus, M Biessy, and D Picart. Dynamic behavior of an aggregate material at simultaneous high pressure and strain rate: SHPB triaxial tests. *International Journal of Impact Engineering*, 38(2-3):73–84, 2011.

[15] R J Christensen, S R Swanson, and W S Brown. Split-Hopkinson bar tests on rock under confining pressure. *Experimental Mechanics*, 12(11):508–513, 1972.

[16] U S Lindholm, L M Yeakley, and A Nagy. The dynamic strength and fracture properties of dresser basalt. *Int. J. Rock Mech. Min. Sci. & Geomech. Abstr.*, 11(5):181–191, 1974.

[17] D J Frew, S A Akers, W Chen, and M L Green. Development of a dynamic triaxial Kolsky bar. *Measurement Science and Technology*, 21(10):105704, 2010.

[18] B E Martin, M E Kabir, and W Chen. Undrained high-pressure and high strain-rate response of dry sand under triaxial loading. *International Journal of Impact Engineering*, 54:51–63, 2013.

[19] Y S Shin, M Lee, K Y Lam, and K S Yeo. Modeling mitigation effects of watershield on shock waves. *Shock and Vibration*, 5(4):225–234, 1998.

[20] J O Hallquist. *LS-DYNA Theory Manual*. Livermore Software Technology Corporation, CA, USA, 2006.

[21] G T Gray III. *Classic split-Hopkinson pressure bar testing*. ASM International, 2000.

[22] D Bancroft. The velocity of longitudinal waves in cylindrical bars. *Physical Review*, 59:588–593, 1941.

[23] A Tyas and D J Pope. Full correction of first-mode Pochhammer-Chree dispersion effects in experimental pressure bar signals. *Measurement Science and Technology*, 16:642–652, 2005.

[24] R M Davies. A critical study of the Hopkinson pressure bar. *Philisophical Transactions of the Royal Society of London, Series A*, 240:375–457, 1948.

[25] A D Barr. *Strain-rate effects in quartz sand*. PhD thesis, The University of Sheffield, 2016.